

Evaluation of the systematic shifts of a $^{40}\text{Ca}^+ - ^{27}\text{Al}^+$ optical clock

Kaifeng Cui^{1,2,‡} · Sijia Chao^{1,2,*} · Chenglong Sun^{1,2,3} · Shaomao Wang^{1,2,3} · Ping Zhang^{1,2,3} · Yuanfei Wei^{1,2,3} · Jinbo Yuan^{1,2} · Jian Cao^{1,2} · Hualin Shu^{1,2} · Xueren Huang^{1,2,4,†}

August 8, 2022

Abstract Quantum-logic-based $^{27}\text{Al}^+$ optical clock has been demonstrated in several schemes as there are different choices of the auxiliary ion species. In this paper, we present the first detailed evaluation of the systematic shift and the total uncertainty of an $^{27}\text{Al}^+$ optical clock sympathetically cooled by a $^{40}\text{Ca}^+$ ion. The total systematic uncertainty of the $^{40}\text{Ca}^+ - ^{27}\text{Al}^+$ quantum logic clock has been estimated to be 7.9×10^{-18} , which was mainly limited by the uncertainty of the quadratic Zeeman shift. By comparing the frequency of two counter-propagating clock beams on the same ion, we measured the frequency stability to be $3.7 \times 10^{-14}/\sqrt{\tau}$.

Keywords Optical clocks · Precision spectroscopy · Quantum metrology

PACS 06.30.Ft · 32.30.Jc · 37.10.Rs

With the rapid development of optical clocks, a new definition of the SI unit of time using the optical clocks has become realistic [1, 2]. Impressed by their high performance, a wide range of applications in the study of fundamental physics [3] such as searching for dark matter [4, 5] or testing general relativity [6, 7], have been proposed. Among all the atomic species, single-ion optical clock based on the $^1\text{S}_0 \leftrightarrow ^3\text{P}_0$ transition on $^{27}\text{Al}^+$ has long been considered as a good candidate [8], not

only because of its 8 mHz narrow linewidth, but also for its very low sensitivity to the black-body radiation (BBR). Recently, research reported the fractional frequency uncertainty of an $^{27}\text{Al}^+$ optical clock reached 9.4×10^{-19} [9], two orders of magnitude better than the best Cesium fountain clock to date [10].

Although optical clocks based on trapped $^{27}\text{Al}^+$ have outstanding performance, they face unique issues in cooling and detection. Due to the lack of commercially available ultraviolet laser at the wavelength of 167 nm, $^{27}\text{Al}^+$ single-ion optical clocks depend on another kind of co-trapped ions to provide sympathetic cooling [11] and quantum logic readout [12]. The first $^{27}\text{Al}^+$ clock was operate with $^9\text{Be}^+$ as auxiliary ion [13] while later the $^{25}\text{Mg}^+ / ^{27}\text{Al}^+$ clock reached the lowest uncertainty to date [9]. Since then, various number of group [14, 15, 16] have started new $^{27}\text{Al}^+$ optical clocks including ours at APM [17, 18].

In this paper, we present a detailed evaluation of an $^{27}\text{Al}^+$ single-ion optical clock sympathetically cooled by a $^{40}\text{Ca}^+$ ion. Comparing to the similar $^{27}\text{Al}^+$ clock sympathetically cooled by $^{25}\text{Mg}^+$ or $^9\text{Be}^+$ at the Doppler cooling limit [13, 19], our result shows a much smaller time dilation shift due to secular motion of the ions, which agrees with the theoretical expectation [20]. We describe the clock system and present the evaluation of the total systematic shift and uncertainty of the clock transition.

We used a linear Paul trap that is similar to the one described previously [21, 17, 18] except for that the radio frequency of the trap is increased to 42.9 MHz for a stronger confinement. To achieve such a high frequency, the electrodes are made of beryllium copper instead of stainless steel for its lower resistance. In order to increase the radio frequency (RF) to 42.9 MHz to avoid heating the excess micromotion sideband, the

¹ Key Laboratory of Atomic Frequency Standards, Innovation Academy for Precision Measurement Science and Technology, Chinese Academy of Sciences, Wuhan 430071.

² State Key Laboratory of Magnetic Resonance and Atomic and Molecular Physics Innovation Academy for Precision Measurement Science and Technology, Chinese Academy of Sciences, Wuhan 430071.

³ University of the Chinese Academy of Sciences, Beijing 100049.

⁴ Wuhan Institute of Quantum Technology, Wuhan 430206

* These authors contribute equally.

‡E-mail: cuikaifeng@apm.ac.cn †E-mail: hxueren@apm.ac.cn.

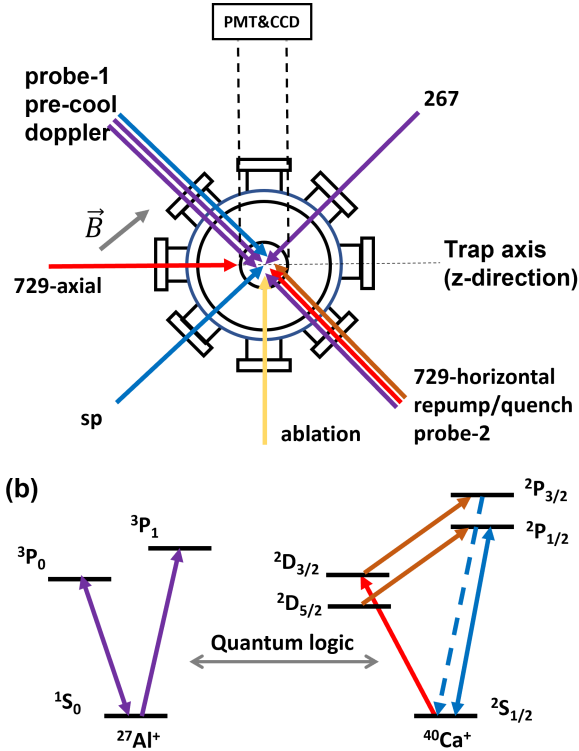


Fig. 1 (a) Laser beams involved in this experiment. A linear Paul trap is placed in the center of the vacuum chamber, with its trap axis along the direction of the 729-axial beam. In addition to the 729-axial and 729-horizontal beams, there is another 729-vertical beam used for the detection of EMM, which is not included in this figure. Fluorescence is collected through an imaging system placed on the vertical direction, sharing the same pathway of the 729-vertical beam. SP indicates the state preparation laser for the $^{40}\text{Ca}^+$ ion, while 267 represents a 267 nm laser that prepares the $^{27}\text{Al}^+$ ion and helps with the quantum logic spectroscopy. Probe-1 and probe-2 are two almost exactly counter-propagating laser beams that excited the clock transition. When alternately interrogated with each of these beams, possible first-order Doppler shift will be cancelled. The stability of the clock is evaluated by comparing the measured frequency of these two beams. (b) Energy levels involved in this experiment (Not to scale).

electrodes are made of beryllium copper for its lower resistance than the stainless steel. The distance between the electrodes to the ion was narrowed to 0.4 mm for stronger confinement. A pair of end-cap electrodes were placed 8.5 mm apart along the trap axis (z-axis). A trap frequency of $(\omega_x, \omega_y, \omega_z) = (4.1, 4.1, 1.1)$ MHz was achieved using this trap.

A Nd: YAG laser at 1064 nm with a maximum pulse energy of 15 μJ and a pulse duration of 2 ns is used for the ablation loading of both $^{40}\text{Ca}^+$ and $^{27}\text{Al}^+$ ions from two separated metal targets. Laser cooling of the $^{40}\text{Ca}^+$ ion is implemented by a 397 nm beam (Doppler beam) that is approximately -10 MHz detuned from resonance. Another 397 nm pre-cool beam with -120 MHz detuning

is co-aligned with the Doppler cooling beam to help the ions recrystallize after collision with the background gas, which happens a few times per hour. A circularly polarized 397 nm laser beam (SP beam) is applied along the magnetic field direction to initialize the $^{40}\text{Ca}^+$ ion to the state $^2\text{S}_{1/2}(m = -1/2)$. A repump beam at 866 nm from the opposite directions pumps the $^{40}\text{Ca}^+$ ion from $^2\text{D}_{5/2}$ state back to the cooling cycle. It is co-aligned with 854 nm laser to pump the ion back to the $^2\text{S}_{1/2}$ state by connecting the $^2\text{D}_{5/2}$ and $^2\text{P}_{3/2}$ state.

In the opposite direction, a pair of 267 nm lasers with orthogonal polarization are co-aligned to initialize $^{27}\text{Al}^+$ to $^1\text{S}_0(m = \pm 5/2)$ state. With the help of another 729 nm laser beam along the trap axis (729-axial beam), the internal state of the $^{27}\text{Al}^+$ can be mapped to the shared motional state by the 267 nm laser and measured out using the quantum logic spectroscopy (QLS) [18]. In addition, we employed two more 729 nm beams (729-horizontal and 729-vertical) to detect the excess micromotion in three directions.

The clock transition is probed from two opposite directions. The first one (probe-1 beam) is co-aligned with the pre-cool beam, and the second one (probe-2 beam) goes together with the repump beam. These two beams are generated from two separate double passed acousto-optic modulators (AOMs). The probe-2 beam is aligned well enough to ensure it goes all the way back through the trap and into the AOM of the probe-1 beam, which proves a deviation of the angle smaller than 2×10^{-5} rad.

Before each $^{27}\text{Al}^+$ clock interrogation pulse, the ions are pre-cooled for 1.5 ms. A series of 267 nm laser pulses are employed at the same time to pump the $^{27}\text{Al}^+$ ion to the $^1\text{S}_0(m_F = \pm 5/2)$ state. Then a Doppler cooling pulse of 1 ms is applied to cool the ions close to the Doppler-cooling limit. The clock interrogation is then applied through either the probe-1 beam or the probe-2 beam. Both the 397 nm Doppler cooling laser and the 866 nm repump laser are kept on during the clock interrogation pulse to ensure that the temperature of the ions remains stable. A sequence of pulses then maps the $^1\text{S}_0$ state of $^{27}\text{Al}^+$ ion to the dark $^2\text{D}_{5/2}(m = -1/2)$ state on $^{40}\text{Ca}^+$ through their shared motional sidebands [18]. The readout process is repeated 5-20 times using an adaptive Bayesian process [22] to reach the lowest measurement error of approximately 0.5%.

At an interrogation time of 25 ms, we observed a clock transition linewidth of 45 Hz [18], which is larger than the Fourier limit of 32 Hz. We believe this is limited by the vibration noise in the laser path since the clock laser beam passed two separate optical tables. For long-term stability, the clock is normally operated at

Table 1 Fractional frequency shifts and uncertainties for the $^{40}\text{Ca}^+ - ^{27}\text{Al}^+$ optical clock in the unit of 10^{-18} .

Effect	Shift	Uncertainty
Quadratic Zeeman	-8617.0	6.4
Secular motion	-6.9	3.1
Excess micromotion	-3.9	2.9
Blackbody radiation	-3.2	0.5
Laser Stark	-1.1	1.1
AOM freq. error	0.0	0.3
First-order Doppler	0.0	0.6
Background-gas collision	0.0	0.2
Total	-8632.2	7.9

an interrogation time of 10 ms, with a clock transition linewidth of $\tilde{80}$ Hz.

The systemic shift is listed in Table 1. The largest shift arises from the influence of the external magnetic field. Considering the first-order and second-order terms in the magnetic field, the resonance frequencies of the clock transition will be shifted to [23]:

$$\nu = \nu_0 + C_1 \langle B \rangle + C_2 \langle B^2 \rangle, \quad (1)$$

where ν_0 is the unperturbed resonance frequency and C_1, C_2 are the coefficient quantifying the linear and the quadratic Zeeman shift, respectively. The first order term $\langle B \rangle$ is compensated by the interleaved locking of two transitions: $^1\text{S}_0(m_F = \pm 5/2) \leftrightarrow ^3\text{P}_0(m_F = \pm 5/2)$, while the second order term, $\langle B^2 \rangle = \langle B_{DC} \rangle^2 + \langle B_{AC}^2 \rangle$ contributes the largest frequency shift. The dominant AC components of the magnetic field is the 50 Hz and harmonics B_{LF} and the trap RF induced oscillating magnetic field B_{RF} . The limited linewidth of the $^1\text{S}_0(m_F = +5/2) \leftrightarrow ^3\text{P}_0(m_F = +5/2)$ transition of the $^{40}\text{Ca}^+$ ion due to the magnetic field noise decoherence is used to infer the lower frequency AC components $B_{LF} = 1.795 \times 10^{-7}$ T.

The oscillating magnetic field B_{RF} modulates the $^2\text{S}_{1/2} \leftrightarrow ^2\text{D}_{5/2}$ transition of the $^{40}\text{Ca}^+$ ion with a modulation index $\beta_m = (g_D m_D - g_S m_S) \mu_B B_{RF} / \hbar \Omega_{RF}$ [24], where g_S, g_D, m_S, m_D are the g-factors and magnetic quantum number of $^2\text{S}_{1/2}$ and $^2\text{D}_{5/2}$ states, respectively, μ_B is the Bohr magneton and \hbar is Planck's constant. However, trap RF induced micromotion, also modulates this transition with index β_0 . The measured Rabi rate ratio η of the carrier and sideband of the transition contains information of both modulation $\eta = (\beta_0 + \beta_m)/2$. The contribution from the micromotion can be removed by using a pair of transitions with different magnetic quantum numbers. In our experiment, the micromotion is first minimized and evaluated as described in the following section. Then the 729-axial beam is employed to measure the Rabi rate ratio of $^2\text{S}_{1/2}(m_S = -1/2) \leftrightarrow ^2\text{D}_{5/2}(m_D = -1/2)$ transition

and $^2\text{S}_{1/2}(m_S = -1/2) \leftrightarrow ^2\text{D}_{5/2}(m_D = -5/2)$ gives $\beta_m = 2.07 \times 10^{-3}$, corresponding to $B_{RF} = 3.67 \times 10^{-6}$ T after taking the projection angle of 729-axial beam into account.

As suggested in Ref. [24], this method may ignore the oscillating magnetic field orthogonal to the quantization axis, results in an underestimate of the total B_{RF} by a factor of 2. Since our current set up does not allow a more precise measurement, we believe taking $B_{RF} = 7.34 \times 10^{-6}$ T provides an upper bound of B_{RF} . With quadratic Zeeman coefficient $C_2 = -7.1944(24) \times 10^7$ Hz/T² [23], the fractional frequency shift due to the AC component of the magnetic field is estimated to be below 1.26×10^{-18} . Since $B_{DC} = 3.6640(12) \times 10^{-4}$ T can be measured with high precision, the total fractional frequency shift due to the quadratic Zeeman effect is $-(8617.0 \pm 6.4) \times 10^{-18}$, limited by the uncertainty of C_2 . It is noticeable that reducing the magnetic field strength $\langle B^2 \rangle$ will lead to significant improvement of the clock performance in the future. Although a much smaller magnetic field increases the coupling to other unwanted Zeeman components in the $^2\text{S}_{1/2} \leftrightarrow ^2\text{D}_{5/2}$ transition of $^{40}\text{Ca}^+$, results in a larger measurement error in the QLS process.

The time dilation shift due to the motion of the $^{27}\text{Al}^+$ ion contributed to most of the uncertainties among all published works on the $^{27}\text{Al}^+$ ion optical clock [19, 9]. There are two types of motions for trapped ions: micromotion that is driven by the trap RF field and harmonic-oscillator (secular) motion at lower frequencies. In both cases, as the ion moves inside an electric field, the total frequency shift needs to include a frequency-dependent term that corresponds to the Stark effect [19]:

$$\frac{\Delta v}{v} = -\frac{E_p}{mc^2} \left(1 + \frac{f}{400\text{MHz}} \right)^2, \quad (2)$$

where E_p and f are the energy and frequency of this motion respectively, and m is the mass of the $^{27}\text{Al}^+$ ion.

The secular motion energy is dominated by laser cooling. All the cooling lasers are kept on during the clock interrogation to ensure the ions stay close to the sympathetic Doppler cooling limit. Consider a clock ion with mass $m_2 = m$ cooled by another ion with mass m_1 , the secular motion energy of the clock ion can be written as:

$$\begin{aligned} E_{\text{SM},i} &= \zeta_i m \omega_i^2 z_i^2 (\bar{n}_i + 1/2) \\ &= \text{TDS}_i (\bar{n}_i + 1/2), \end{aligned} \quad (3)$$

where TDS_i stand for the calculated value representing the time dilation shift per quantum number. ζ_i is a factor that describes the intrinsic micromotion (IMM) driven by the trapping RF field. $z_i = b_i z_{0,i}$ is the mode

Table 2 One of the measurement results of the average motional quantum number \bar{n}_m that is used to calculate the corresponding time-dilation shift. z stands for the amplitude of the motion at the ground state. \bar{n}_c is the calculated average motional quantum number at Doppler cooling limit. TDS/quantum is the calculated time-dilation shift per quantum number that has included the contribution of intrinsic micromotion. For this particular measurement, the time-dilation shift is 8.34×10^{-18} . We made several measurements on different days and take the average as our final result.

Mode	\hat{x} -COM	\hat{x} -STR	\hat{y} -COM	\hat{y} -STR	\hat{z} -COM	\hat{z} -STR
Frequency(MHz)	4.00	2.84	4.03	2.84	1.17	2.10
z (nm)	6.6	0.6	6.4	0.5	7.1	7.8
\bar{n}_m	5.2	7.0	3.0	5.7	12.8	7.5
\bar{n}_c	3.0	4.6	3.0	4.6	7.3	4.0
TDS/quantum(10^{-18})	0.747	0.004	0.757	0.003	0.030	0.118
Total TDS(10^{-18})	3.94	0.03	2.29	0.02	0.39	0.89

amplitude of this motion at the ground state, ω_i is the mode frequency, $z_{0,i} = \sqrt{\hbar/(2m_2\omega_i)}$, b_i is the component of the normalized eigenvector for the mode [20], and \bar{n}_i is the average motional quantum number that can be measured by comparing the amplitude of the red and blue sidebands [17]:

$$\bar{n}_i = \frac{P_{r,i}}{P_{b,i} - P_{r,i}}. \quad (4)$$

The IMM has a frequency exactly the same as that of the driven field and exists even in an ideal Paul trap. The energy of the IMM is approximately the same as the secular energy in the transverse direction for a single ion. For two co-trapped ions, ζ_i can be expressed as [20]:

$$\zeta_{i,\text{COM}} = 1 + \frac{2\epsilon^2/\mu}{2\epsilon^2/\mu - 2\alpha - (1 - \sqrt{\mu}b_1/b_2)}, \quad (5)$$

$$\zeta_{i,\text{STR}} = 1 + \frac{2\epsilon^2/\mu}{2\epsilon^2/\mu - 2\alpha - (1 + \sqrt{\mu}b_2/b_1)}. \quad (6)$$

COM and STR indicate for center-of-mass mode and stretch mode, respectively. $\mu = m_2/m_1$, $\alpha \approx 0.622$ and $\epsilon \approx 2.778$ are geometric parameters for the trapping field.

We took several measurements in different days and used the weighted average $-(6.9 \pm 3.1) \times 10^{-18}$ as the final result. The uncertainty is given by twice of the standard deviation of the measurements and is shown in the gray band in Fig. 2 (a). One of these measurements is shown in Table 2. The secular motion energy at this cooling limit can be calculated [20]:

$$E_{i,\text{limit}} = \frac{\hbar\Gamma}{24} \frac{2(1 + 3l_i^2)}{l_i^2}, \quad (7)$$

where $\Gamma = 20.4$ MHz is the natural linewidth of the $^2\text{S}_{1/2} \rightarrow ^2\text{P}_{1/2}$ transition on $^{40}\text{Ca}^+$ that is used for the Doppler cooling. l_i represents the projection of the cooling laser to i -th direction. The calculated cooling limited is listed as \bar{n}_c in Table 2. It can be seen that our clock was operated close to this Doppler cooling limit. This corresponding to a time dilation shift of

-6.3×10^{-18} , lower than a similar $^{27}\text{Al}^+$ clock that symmetrically cooled by $^{25}\text{Mg}^+$ [19]. The accuracy of the measurement is limited by the decoherence due to magnetic field noise since it reduces $P_{b,i}$ and $P_{r,i}$. Cooling the ions much closer to the motional ground states will leads to a higher $P_{b,i}$ and a lower $P_{r,i}$, results in a stronger resistance to the decoherence. Due to a suitable mass ratio between $^{40}\text{Ca}^+$ and $^{27}\text{Al}^+$ ions, we note that two of these motional modes have much smaller amplitude and therefore contribute less to the motional energy of the $^{27}\text{Al}^+$ ion. This makes it easier to reduce the time-dilation shift due to the secular motion through ground state cooling in the future.

In addition to the IMM, the ion may suffer from additional kinetic energy arising from the imperfection of the trapping potential or phase shifts between the trap electrodes. This causes the excess micromotion and its energy E_{EMM} can be measured through the ratio of the Rabi rate of the carrier and the EMM sideband η [25]:

$$E_{\text{EMM}} = \sum_i \frac{m\Omega_{RF}^2\eta_i^2}{k_L^2c^2}, \quad (8)$$

i is summed over all three perpendicular directions, and k_L is the wave vector of the detection laser beam.

Our measurement of E_{EMM} is performed on the $^{40}\text{Ca}^+$ ion ($m_{\text{Ca}} = m_1$) using three different 729 nm laser beams. The vertical (729-vertical) and axial (729-axial) beam are perpendicular to each other, while the horizontal beam (729-horizontal) is at 45° angles to the axial beam (Fig. 1). Taking this into account, the frequency shift on $^{27}\text{Al}^+$ ion can be written as:

$$E_{\text{EMM}} = \sum_i \frac{m_1^2\nu_{RF}^2}{m_2\nu_1^2} (\chi_i\eta_i)^2, \quad (9)$$

where $\nu_1 \approx 411.042$ THz represents the frequency of the detection laser that excited the $^2\text{S}_{1/2} \rightarrow ^2\text{D}_{5/2}$ transition of the $^{40}\text{Ca}^+$ ion. χ_i denotes a factor that describes the projection of laser direction.

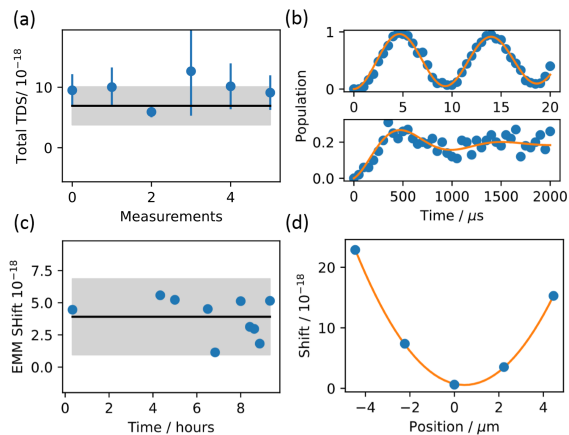


Fig. 2 Measurements of the time-dilation shift. (a) Time-dilation shift due to SM and related IMM measured over several days. We took the weighted average as the final result and estimated the uncertainty of this measurement as twice of the standard deviation. (b) An example of the Rabi flopping on the carrier (top panel) and the micromotion sideband (bottom panel) on the $^{40}\text{Ca}^+$ ion driven by the 729-vertical beam. (c) Average EMM frequency shift measured during a day. The clock is free-running without an EMM servo after the initial EMM compensation. Moreover, the order of our ion pair is not controlled. The final EMM frequency shift is $-(3.9 \pm 2.9) \times 10^{-18}$, where the uncertainty is given by twice of the standard deviation, and is shown in the gray band. (d) EMM shift along the trap axis. As we did not control the order of the $^{40}\text{Ca}^+$ and $^{27}\text{Al}^+$ ions, we tried to arrange the ions symmetrically around the minimal micromotion point.

During the clock operation, we started from minimizing the EMM shift by adjusting the compensation voltages, and left it free-running for the rest of the day. Therefore, we continued measuring the EMM shift throughout the entire day and found the total frequency shift due to EMM by averaging those data, yielding a result of $-(3.9 \pm 2.9) \times 10^{-18}$. The uncertainty is given by twice of the standard deviation, as shown in the gray band in Fig. 2 (c).

In a perfect linear Paul trap, EMM does not exist along the trap axis. However, our trap is not perfect, as we observed a minimum axial EMM at a special location (Fig. 2 (d)). It's hard to keep the $^{27}\text{Al}^+$ ion staying at this point because random background-gas collision switched the order of the $^{40}\text{Ca}^+ - ^{27}\text{Al}^+$ pair approximately every 1000 s. We did not control the order of the ions, instead, we moved the center of the ion pair close to this minimum point and left it free running. We observed some reorder events during the clock operation, and the EMM measurements were taken in both orders randomly. Other sources that lead to a change of the EMM, such as ion reloading or charging due to the clock laser [9] are not evident in our case since the change of the $^{27}\text{Al}^+$ ion's position due to reordering event is the dominant effect.

The reorder events are recorded and used to evaluate the collision shift for the background gas. The energy that is required by the $^{40}\text{Ca}^+ - ^{27}\text{Al}^+$ ions to change their order is given by [26]:

$$E_{reorder} = \frac{3}{4} \left(\frac{\sqrt{m}\omega_z e^2}{2\pi\epsilon_0} \right)^{2/3} \times \left(\left\{ \frac{2(\epsilon^2 + \alpha - 1)[\epsilon^2 + \mu(\alpha - 1)]}{\epsilon^2(\mu + 1) + 2\mu(\alpha - 1)} \right\}^{1/3} - 1 \right), \quad (10)$$

where e is the charge of the electron. α, ϵ are geometric factor that associate with the trap itself. $\mu = m_2/m_1$ is the ratio of $^{27}\text{Al}^+$ and $^{40}\text{Ca}^+$ ion's mass. The relationship between the vacuum pressure and the reorder rate is given by:

$$\Gamma_{reorder} \lesssim \frac{1}{2} \left(\frac{p}{902\text{nPa}} \right) \left(\frac{E_{reorder}}{1\text{K} \times k_B} \right). \quad (11)$$

The reorder event can be easily observed on the EMCCD camera since the position of the $^{40}\text{Ca}^+$ ion is shown as a bright while the $^{27}\text{Al}^+$ ion is invisible. We took an image from the EMCCD every 0.5 s and averaged 10 images to reduce noise from the background. This averaging normally does not miss any reorder events, as the reorder period is around 1000 s, much longer than the imaging time. The geometric center of the measured $^{40}\text{Ca}^+$ ion was recorded to determine the position of the ion.

The reorder rate is given by $\Gamma_{reorder} = N_{reorder}/T$, where $N_{reorder}$ is the number of reorder events during time T . In our case, the reorder rate was measured to be $\Gamma_{reorder} = 0.0013 \text{ s}^{-1}$, corresponding to a vacuum pressure of 3.8 nPa. Based on an empirical formula from Rosenband et al. [13], and assuming that each collision brings a maximum phase shift of $\pi/2$, background gas collision leading a frequency shift up to 0.195 mHz, corresponding to a fractional frequency shift of 0.2×10^{-18} . We take this value as the uncertainty of this effect.

The blackbody radiation (BBR) leads to an AC Stark shift in the clock transition. The $^{27}\text{Al}^+$ clock is operated at room temperature ($\approx 300 \text{ K}$), The BBR temperature is mainly caused by the thermal radiation emitted from various components of the ion trap. We built another ion trap system with the same configuration to achieve an accurate assessment of the BBR temperature using an infrared thermal imager. Temperature sensors were placed on both this trap and the actual system to ensure that they work in the same condition. The finite element analysis method was also employed to achieve an accurate assessment of the BBR temperature [27]. For the $^{27}\text{Al}^+$ ion, the effective BBR

Table 3 The result of the systemic shift due to black-body radiation (BBR) of the ion trap system.

Components	Ω_{eff}	Value (K)	Uncertainty (K)	Uncertainty T_{eff} (K)
Blade electrodes	0.457	303.87	2.90	0.110
Cap electrodes	0.293	304.16	2.59	0.064
Insulation supports	2.284	302.78	2.58	0.488
Compensation electrodes	0.245	304.07	2.65	0.055
Stainless steel brackets	0.675	302.78	2.21	0.128
Chamber	1.264	297.97	1.43	0.169
Glass Windows	6.016	297.97	1.43	0.801
Flanges	1.333	297.97	1.43	0.178

temperature can be calculated using:

$$T_{eff} = \sqrt[4]{\sum_i \frac{\Omega_{eff} T_i^4}{4\pi}}, \quad (12)$$

where Ω_{eff} and T_i are the effective solid angle and temperature of each component of the trapped ion system listed in Table 3. This gives $T_{eff} = 299.6$ (1.0) K. We noticed that there is a temperature difference of 0.94K between the simulation trap and the actual trap when driving with the same RF field. Taking that into consideration, the effective BBR temperature felt by the ion is estimated to be $T_{eff} = 299.6 \pm 1.4$ K. The clock frequency shift due to BBR is calculated using [9]:

$$\Delta\nu_{BBR} = -\frac{\pi\Delta\alpha_0}{60\epsilon_0c^3} \left(\frac{k_B^4 T_{eff}^4}{h^4} \right)^4, \quad (13)$$

where $\Delta\alpha_0 = 7.03(94) \times 10^{-42}$ Jm²/V² is the static differential polarizability. The corresponding BBR shift is $-(3.2 \pm 0.5) \times 10^{-18}$.

The electric field of the optical radiation incident on the ion perturbs and shifts the line center of the ion transition. This contributes to the Stark shift [9]:

$$\Delta\nu_{ac} = -\frac{\Delta\alpha_{ac}(\lambda)}{2hc\epsilon_0} I, \quad (14)$$

where $\Delta\alpha_{AC}(\lambda)$ is the dynamic polarizability of the wavelength λ and I is the intensity of the incident light. The intensity of the clock laser was measured to be 40 nW, focused on an area of 120 μ m in diameter, corresponding to an AC Stark shift $(0.0 \pm 0.1) \times 10^{-18}$.

In addition to the clock laser itself, both the 397 nm cooling light and the 866 nm pumping light are present during clock operation. The intensities of both beams are calibrated by monitoring the fluorescence of the ions periodically during the clock operation. We noticed that the fluorescence will change significantly if the power of the 397 nm laser exceeds 34 nW. With a measured beam waist of 80 μ m, this lead to an AC stark shift up to -1.3×10^{-19} . Since the 866 nm beam and the 729-horizontal beam share the same fiber and optics, the waist position of these beams are different due

to the optical dispersion. To ensure the 729-horizontal beam has the strongest coupling with the ion, the ion have to stay approximately 100 μ m off from the 866 nm beam waist. This leads to a much higher requirement of the 866 nm laser power, reaching 7.4 μ W. We checked the possible maximum laser intensity around the ion (within a range of 20 μ m \times 20 μ m) using beam profiler and figured out the maximum possible AC stark shift for the 866 nm laser can reach -9.4×10^{-19} . In summary, the total AC Stark shift due to these three lasers is smaller than 1.1×10^{-18} .

Phase chirp in the clock beam AOM can also contribute to a frequency shift as the optical path through the crystal changes when it switches on and off. The shift due to a phase chirp is minimized by using a very lower RF driving power (1.1 mW) on the AOM [13]. This lead to a shift smaller than 0.3×10^{-18} .

The first-order Doppler shift cannot be observed for most optical clocks that work in the Lamb-Dicke regime because the motional amplitude is much smaller than the laser wavelength. However, a first-order Doppler shift may still occur when the ion itself moves in a fashion correlated with the clock laser. This movement may come from the contraction of the structure of the ion trap or an additional electric field generated by the UV photoelectric effect. We compared the output frequency of the counter-propagating probe-1 and probe-2, looking for the first order Doppler shift. No statistical frequency difference can be observed with a fractional uncertainty of 5.4×10^{-17} . Interleaved detection is employed during the comparison to show the Rabi line-shape seen from these two directions (Fig. 3 (b)). When the average frequencies of these two directions are used as the output of the clock, possible first order Doppler shift can be further canceled. However, due to the drift of the laser locking on the cavity, and the imperfectly matched laser intensity, a residual frequency shift may arise from the imbalanced transition probabilities of the left and right sides of the peak [13]. This lead to a frequency shift smaller than 0.6×10^{-19} , limited by the servo error of these two feedback loops.

The instability of the comparison is calculated from the measured frequency difference, shown in black dots

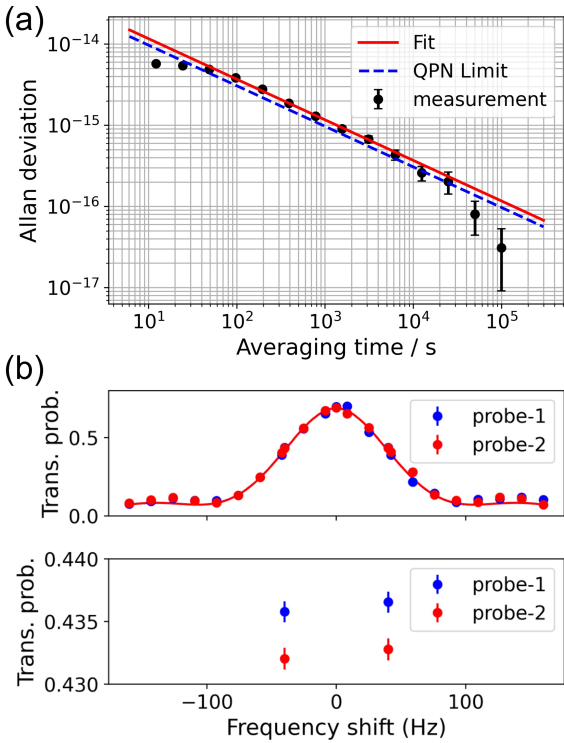


Fig. 3 (a) The stability of the clock determined from comparing the output frequency of laser beam probe-1 and probe-2. The data was taken after an operation time of $\hat{1}60$ hours, with a duty cycle of 48%. Red line is a fit using $\sigma_y/\sqrt{\tau}$ while $\sigma_y = 3.7 \times 10^{-14}$. The quantum projection noise (QPN) is shown in blue dashed trace, $\sigma_{QPN} = 3.2 \times 10^{-14}$, has taken account into the effect from the loss of contrast due to the decoherence from the vibrational noise of the laser path. (b) Interleave detection is employed during the comparison to visualize the locked line-shape from both laser beam directions. The lower panel is a zoom in of the transition probability of the left and right side of the peak. The unbalanced probabilities suggested a residual first order Doppler shift from the drifting laser, which is smaller than 0.6×10^{-19} .

in Fig.3 (a). Fitting of these data points gives $\sigma_y(\tau) = 3.7 \times 10^{-14}/\sqrt{\tau}$ and marked as a red line. The experiment lasted for $\hat{1}60$ hours, with a duty cycle of 48%. Although the $^{40}\text{Ca}^+ - ^{27}\text{Al}^+$ ion pair can remind in the trap for several days without running the experiment, probing the $^1\text{S}_0 \leftrightarrow ^3\text{P}_0$ transition will shorten the lifetime of the $^{27}\text{Al}^+$ ion to approximately 2 hours. This is because the $^{27}\text{Al}^+$ ion has a much higher possibility of reacting with background hydrogen molecules when excited in the $^3\text{P}_0$ state. Reloading and calibrating process cost $\hat{2}0$ minutes when an aluminum hydride molecule is formed. However, laser drifts, especially the drift from the cooling lasers require manual adjustments during the lock, which now limits the improvements of the duty cycle time.

In summary, we have evaluated the fractional frequency shift and associated systematic uncertainty for an $^{27}\text{Al}^+$ clock sympathetically cooled by a $^{40}\text{Ca}^+$ ion. The total shift is $-(8632.2 \pm 7.9) \times 10^{-18}$. The systematic uncertainty is limited by the quadratic Zeeman shift, which is mainly caused by the measurement uncertainty of the quadratic Zeeman coefficient C_2 . Significant improvements can be made when the magnetic field $\langle B \rangle$ is reduced in the future. Our measurement of the secular motion temperature is also limited by decoherence from magnetic field noise and jitter on the amplitude of the RF trapping field. In addition, controlling the order of the ions is inevitable that the uncertainty of time dilation shift due to excess micromotion can be improved. Owing to the relatively lower Doppler cooling limit from the $^{40}\text{Ca}^+$ ion and the suitability mass ratio to $^{27}\text{Al}^+$ ion, we achieved a lower time-dilation shift due to secular motion than that of a $^{25}\text{Mg}^+ - ^{27}\text{Al}^+$ clock. As the $^{40}\text{Ca}^+$ ion has a suitable energy level for electromagnetically-induced-transparency (EIT) cooling, it is possible to bring the motional energy much closer to the motional ground state to reduce the time-dilation shift due to the motion. Benefits from its simple laser system [28], optical clocks based on $^{40}\text{Ca}^+ - ^{27}\text{Al}^+$ ions have the potential to achieve a transportable, compact design.

Author contribution

S.W, J.C, H.S and X.H developed components of the experimental apparatus. P.Z, Y.W evaluated the black-body radiation shifts. K.C, S.C, C.S, Y.W and J.Y collected and analyzed most of the data. All authors discussed the results and contributed to the writing of the paper.

Data availability

The datasets generated during and/or analysed during the current study are available from the corresponding author on reasonable request.

Acknowledgements We thank M. Zhan and C. Li for useful discussions. This work is supported by the National Key R&D Program of China (Grant No. 2017YFA0304401), the Strategic Priority Research Program of the Chinese Academy of Sciences (Grant No. XDB21030100), the Technical Innovation Program of Hubei Province (Grant No. 2018AAA045) and the National Natural Science Foundation of China (Grant No. 11904387, U21A20431).

References

1. F. Riehle, *Comptes Rendus Physique* **16**(5), 506 (2015)
2. J. Lodewyck, *Metrologia* **56**(5), 055009 (2019)
3. M.S. Safronova, D. Budker, D. DeMille, D.F.J. Kimball, A. Derevianko, C.W. Clark, *Rev. Mod. Phys.* **90**(2), 025008 (2018)
4. C.J. Kennedy, E. Oelker, J.M. Robinson, T. Bothwell, D. Kedar, W.R. Milner, G.E. Marti, A. Derevianko, J. Ye, *Phys. Rev. Lett.* **125**(20), 201302 (2020)
5. P. Wcislo, P. Ablewski, K. Beloy, S. Bilicki, M. Bober, R. Brown, R. Fasano, R. Ciuryło, H. Hachisu, T. Ido, J. Lodewyck, A. Ludlow, W. McGrew, P. Morzyński, D. Nicolodi, M. Schioppo, M. Sekido, R.L. Targat, P. Wolf, X. Zhang, B. Zjawin, M. Zawada, *Sci. Adv.* **4**(12), eaau4869 (2018)
6. C.W. Chou, D.B. Hume, T. Rosenband, D.J. Wineland, *Science* **329**(5999), 1630 (2010)
7. M. Takamoto, I. Ushijima, N. Ohmae, T. Yahagi, K. Kokado, H. Shinkai, H. Katori, *Nat. Photonics* **14**(7), 411 (2020)
8. N. Yu, H. Dehmelt, W. Nagourney, *Proc. Natl. Acad. Sci. USA* **89**(16), 7289 (1992)
9. S.M. Brewer, J.S. Chen, A.M. Hankin, E.R. Clements, C.W. Chou, D.J. Wineland, D.B. Hume, D.R. Leibbrandt, *Phys. Rev. Lett.* **123**(3), 033201 (2019)
10. S. Weyers, V. Gerginov, M. Kazda, J. Rahm, B. Lipphardt, G. Dobrev, K. Gibble, *Metrologia* **55**(6), 789. Publisher: IOP Publishing
11. D. Kielpinski, B.E. King, C.J. Myatt, C.A. Sackett, Q.A. Turchette, W.M. Itano, C. Monroe, D.J. Wineland, W.H. Zurek, *Phys. Rev. A* **61**(3), 032310 (2000)
12. P.O. Schmidt, T. Rosenband, C. Langer, W.M. Itano, J.C. Bergquist, D.J. Wineland, *Science* **309**(5735), 749 (2005)
13. T. Rosenband, D.B. Hume, P.O. Schmidt, C.W. Chou, A. Brusch, L. Lorini, W.H. Oskay, R.E. Drullinger, T.M. Fortier, J.E. Stalnaker, S.A. Diddams, W.C. Swann, N.R. Newbury, W.M. Itano, D.J. Wineland, J.C. Bergquist, *Science* **319**(5871), 1808 (2008)
14. M. Guggemos, D. Heinrich, O.A. Herrera-Sancho, R. Blatt, C.F. Roos, *New J. Phys.* **17**(10) (2015)
15. S. Hannig, L. Pelzer, N. Scharnhorst, J. Kramer, M. Stepanova, Z.T. Xu, N. Spethmann, I.D. Leroux, T.E. Mehlstäubler, P.O. Schmidt, *Rev. of Sci. Inst.* **90**(5), 053204 (2019). Publisher: American Institute of Physics
16. Z. Ma, H. Liu, W. Wei, W. Yuan, P. Hao, Z. Deng, H. Che, Z. Xu, F. Cheng, Z. Wang, et al., *Appl. Phys. B* **126**(8), 1 (2020)
17. K.F. Cui, J.J. Shang, S.J. Chao, S.M. Wang, J.b. Yuan, P. Zhang, J. Cao, H.L. Shu, X.R. Huang, *J. Phys. B: At. Mol. Opt. Phys.* **51**(4), 045502 (2018)
18. S.J. Chao, K.F. Cui, S.M. Wang, J. Cao, H.L. Shu, X.R. Huang, *Chinese Phys. Lett.* **36**(12), 120601 (2019)
19. C.W. Chou, D.B. Hume, J.C.J. Koelemeij, D.J. Wineland, T. Rosenband, *Phys. Rev. Lett.* **104**(7), 070802 (2010)
20. J.B. Wubbena, S. Amairi, O. Mandel, P.O. Schmidt, *Phys. Rev. A* **85**(4), 043412 (2012)
21. J.J. Shang, K.F. Cui, J. Cao, S.M. Wang, S.J. Chao, H.L. Shu, X.R. Huang, *Chin. Phys. Lett.* **33**(10), 103701 (2016)
22. D.B. Hume, T. Rosenband, D.J. Wineland, *Phys. Rev. Lett.* **99**(12), 4 (2007)
23. S.M. Brewer, J.S. Chen, K. Beloy, A.M. Hankin, E.R. Clements, C.W. Chou, W.F. McGrew, X. Zhang, R.J. Fasano, D. Nicolodi, H. Leopardi, T.M. Fortier, S.A. Diddams, A.D. Ludlow, D.J. Wineland, D.R. Leibbrandt, D.B. Hume, *Phys. Rev. A* **100**(1), 013409 (2019)
24. H.C.J. Gan, G. Maslennikov, K.W. Tseng, T.R. Tan, R. Kaewuam, K.J. Arnold, D. Matsukevich, M.D. Barrett, **98**(3), 032514. Publisher: American Physical Society
25. D.J. Berkeland, J.D. Miller, J.C. Bergquist, W.M. Itano, D.J. Wineland, *J. Appl. Phys.* **83**(10), 9 (1998)
26. A.M. Hankin, E.R. Clements, Y. Huang, S.M. Brewer, J.S. Chen, C.W. Chou, D.B. Hume, D.R. Leibbrandt, *Phys. Rev. A* **100**(3), 033419 (2019)
27. P. Zhang, J. Cao, J.B. Yuan, D.X. Liu, Y. Yuan, Y.f. Wei, H.l. Shu, X.R. Huang, *Metrologia* **58**(3), 035001 (2020)
28. J. Cao, J. Yuan, S. Wang, P. Zhang, Y. Yuan, D. Liu, K. Cui, S. Chao, H. Shu, Y. Lin, S. Cao, Y. Wang, Z. Fang, F. Fang, T. Li, X. Huang, *Appl. Phys. Lett.* **120**(5), 054003 (2022)